

Electron Beam Synthesis of Metal and Semiconductor Nanoparticles Using Metal-Organic Frameworks as Ordered Precursors

Benjamin W. Jacobs,¹ Ronald J. T. Houk,¹ Bryan M. Wong,¹ A. Alec Talin,² and Mark D. Allendorf^{1,*}

¹Sandia National Laboratories, Livermore, CA 94550, USA, ²Center for Nanoscience and Technology, National Institute of Standards and Technology, Gaithersburg, MD 20899, USA

RECEIVED DATE (automatically inserted by publisher); mdallen@sandia.gov

ABSTRACT: We demonstrate a versatile, bottom-up method of forming metal and semiconducting nanoparticles by exposing precursor metal-organic frameworks (MOFs) to an electron beam. Using a transmission electron microscope to initiate and observe growth, we show that the composition, size, and morphology of the nanoparticles are determined by the chemistry and structure of the MOF, as well as the electron beam properties. Indium, copper, and zinc oxide particles were produced with narrow and tunable size distributions comparable to those obtained from state-of-the-art methods. This method represents a first step toward fabrication of nanoscale heterostructures using the highly controlled environment of the MOF pores as a scaffold or template.

The unique, size-dependent properties of metallic and semiconducting nanoparticles are generating enormous interest in using these materials for applications ranging from electronics to catalysis and bio/medicine.¹ However, control over size, shape, and assembly of such small particles, which is essential for both uniform properties and device fabrication, remains a significant challenge. Current fabrication routes using solution, templating, and top-down approaches all have significant limitations, particularly in the < 10 nm size range where intriguing quantum-mechanical effects are displayed.²

A recent innovation that produces extremely small particles was described by Fischer et al., in which metal-organic frameworks (MOFs) are infiltrated with organometallic precursors, then “developed” using thermal, photolytic, or chemical reduction methods.³ MOFs are crystalline materials composed of metal ions or clusters connected by organic ligands to create a rigid framework. This structure is advantageous as a template because it provides considerable flexibility to tune both pore size and chemical environment, and an extensive library of MOFs now exists. The nanoparticles resulting from MOF infiltration are on the order of the pore dimensions (typically < 2 nm) and are chemically stabilized by the framework. We and others⁴ extended this concept by using metal salts to create silver and gold nanoparticles as small as Ag₃.⁵ Unfortunately, since very few MOFs with pore sizes ≥ 2.5 nm exist, a wide range of potentially interesting particle sizes are inaccessible.

Here, we demonstrate an alternative approach in which the MOF itself is the precursor to particle formation. Recently, we showed that exposing silver-infiltrated MOF templates to an electron beam leads to rapid framework breakdown and subsequent Ag coalescence. Depending on the MOF structure, either nanoparticles in the 2 nm – 6 nm size range or arrays of nanowires can be created.^{5,6} Interestingly, the metal ions

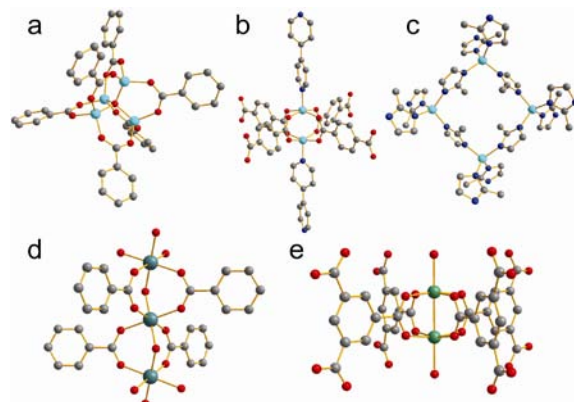


Figure 1. a) IRMOF-1 SBU (IR-Isorecticular; SBU-secondary building unit). b) MOF-508 SBU c) ZIF-8 SBU d) Cu(BTC) SBU e) MIL-68(In) SBU. Grey: carbon; red: oxygen; aqua: zinc; blue: nitrogen; green: copper; teal: indium.

composing the framework are captured within the amorphous decomposition matrix and do not form individual nanoparticles (for example, no Zn-containing particles are detected following exposure of Ag@MOF-508 to the electron-beam). In this work we show that electron-beam (e-beam) decomposition of neat MOFs can be used to create both metal and metal-oxide nanoparticles. Although e-beams have been used to form nanoparticles,^{7,8} nanowires,⁹ and modify the electrical properties of materials,¹⁰ MOFs as precursors offer several important advantages. First, particle size can be controlled by beam current, leading to particles as small as 1.2 nm with very narrow size distributions, but also larger particles (up to 100 nm). Second, the remaining carbonaceous linker material from the MOF acts as a matrix to prevent further coalescence, agglomeration, and oxidation. Finally, since MOFs can be grown on surfaces,¹¹ the extremely high spatial resolution afforded by electron-beam methods, coupled with the well-defined MOF unit cell dimensions, creates potential for bottom-up self assembly with feature sizes in the single-digit nm range. In this work we explore these concepts, using a transmission electron microscope (TEM) to both initiate nanoparticle self assembly and obtain real-time, in-situ information concerning the nucleation, growth, and diffusion processes.

The type and morphology of e-beam induced nanoparticles is determined by at least four factors: (1) the oxidation potential of the MOF metal centers; (2) the ligands in the coordination sphere surrounding the metal center and the strength of the bonds; (3) the coordination sphere geometry; and (4) the e-beam conditions. Five MOFs were used to systematically determine characterize the influence of these parameters. The selected MOFs encompass a range of representative structures and chemistries. Three Zn-

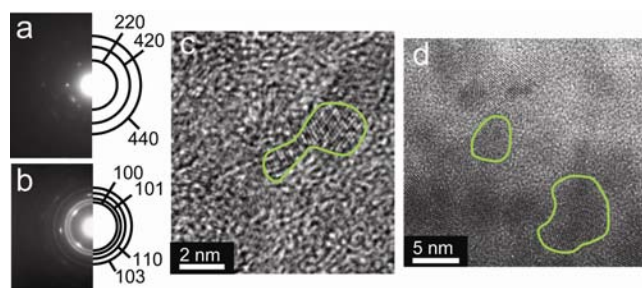


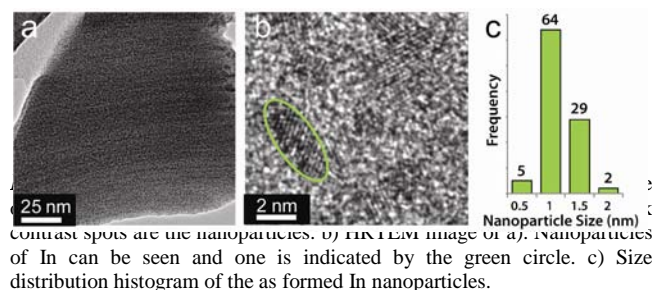
Figure 2. ZnO formation in IRMOF-1. a) Electron diffraction pattern of the intact MOF. b) Electron diffraction pattern of MOF after electron beam irradiation. Pattern corresponds to wurtzite ZnO. c) HRTEM image of ZnO nanoparticles embedded in the decomposed framework after irradiation in the 400 kV microscope.

based MOFs, IRMOF-1, MOF-508 and ZIF-8 (Figure 1a-c) were used to investigate the formation of Zn-based materials, such as ZnO, and to probe the effects of coordination environment. IRMOF-1 has tetrahedral Zn_4O clusters connected by 1,4-benzenedicarboxylic acid (BDC, terephthalic acid) and enclosed pores.¹² MOF-508 has a mixed coordination sphere, in which 2-D sheets are formed from Zn(II) ions in a paddlewheel arrangement, coordinated by BDC linkers in the plane and 4,4'-dipyridyl (bipy) pillar ligands perpendicular to the plane.¹³ Finally, ZIF-8 (zeolitic imidazolate framework) has tetrahedral coordination by the nitrogens of imidazolate linkers, leading to a sodalite structure with enclosed pores.¹⁴ The two remaining MOFs, indium MOF MIL-68(In) and the copper-containing MOF Cu(BTC) (Figures 1d and 1e), allow us to probe the dependence of metal center and oxidation potential on the type of nanoparticles that form, while maintaining a carboxylate-based coordination sphere. MIL-68(In) is composed of infinite 1-D chains of In atoms linked with BDC,¹⁵ and has open 1-D channels. Cu(BTC), also known as HKUST-1, has a primitive cubic structure in which Cu(II) is coordinated to benzenetricarboxylic acid (BTC, trimesic acid) in a paddlewheel geometry, forming enclosed pores connected by smaller pore apertures.¹⁶ The oxidation potentials for Cu(II) and In(III) are 0.34 eV and 0.34 eV vs. standard hydrogen electrode (SHE), respectively, compared with 0.76 eV vs. SHE for Zn(II). All MOF materials were synthesized as described in the literature (see supporting information).

Two TEMs with different current densities and beam energies were used to initiate nanoparticle growth and observe the resulting nanoparticle morphology. A JEOL 2010F with a field-emission source operating at 200 kV and a small beam current (10.3 A m^{-2}) was used to irradiate MOFs, observe degradation in real time, and perform elemental analysis. The effect of higher current densities was probed using a JEOL 4000EX with a LaB_6 source operating at 400 kV. The current density is much higher in this instrument (730 A m^{-2}), but because of the higher accelerating voltage the actual energy deposition in the sample is lower by $\approx 22\%$, as determined from the Bethe equation.¹⁷

The results of exposing the three Zn-based MOFs to the e-beam demonstrate that ZnO nanoparticles form and their size can be tuned using the e-beam current density. When IRMOF-1 is exposed to the 200 kV electron beam, ZnO nanoparticles readily form. As seen in Figure 2a, the SAED pattern of IRMOF-1 obtained after a few seconds in the beam indicates the MOF structure is intact for ≈ 30 s, due to the lower current density when the beam is defocused for this measurement. Under normal imaging conditions, however, the SAED pattern disappears after roughly 10 s, and after approximately 2 min ZnO nanoparticles are visible (Figure 2c). These nanoparticles are consistently very

small, on the order of 1 nm^{-3} nm in diameter. A diffraction pattern could not be obtained for this sample, presumably because these particles are too small to significantly diffract. In contrast, after 60

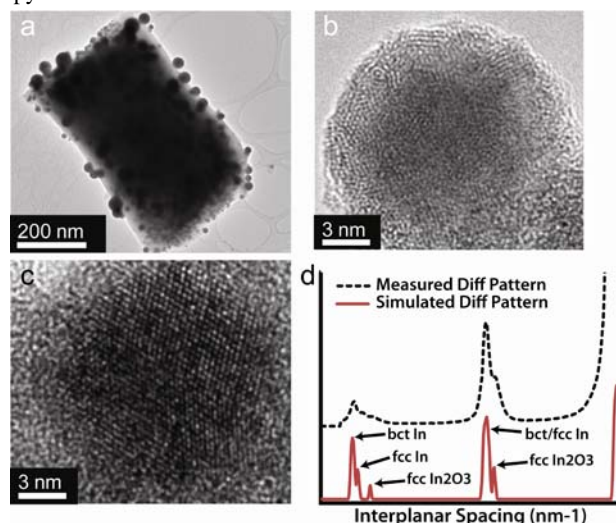


s in the 400 kV beam, much larger, crystalline ZnO nanoparticles form, as shown by the SAED pattern corresponding to the wurtzite structure of ZnO (Figure 2b). Spots in this pattern may indicate preferential growth directions or large single crystal particles, but neither are directly observed. The post-exposure high resolution TEM (HRTEM) image in Figure 2d shows an array of 3 nm to 7 nm ZnO nanoparticles embedded in an amorphous matrix.

The IRMOF-1 transformation to ZnO is confirmed with micro Raman and photoluminescence (PL) spectroscopy, collected before and after exposure to the 400 kV e-beam. The PL spectra of the unexposed and exposed IRMOF-1, as well as the neat BDC linker, are compared in Figure S1. Weak bands visible in the luminescence spectrum of the exposed MOF correspond to the unexposed IRMOF-1 and BDC, indicating very little intact MOF remains. A new band is observed at 507 nm that is consistent with emission from deep-level traps from oxygen vacancies in nanocrystalline ZnO.^{18,19, 20} However, an accurate size distribution is difficult to obtain from the TEM images due to poor contrast. The composition of the amorphous matrix surrounding the particles is primarily elemental carbon, as indicated by micro-Raman spectroscopy (Figure S2). Vibrational modes from the linker and unexposed MOF spectra are not present in the spectrum of the exposed sample, but the broad peaks at 1345 cm^{-1} and 1606 cm^{-1} are attributed to amorphous and graphite-like carbon, respectively.²¹ This carbonaceous material evidently serves as a stabilizing matrix, preventing further coalescence and agglomeration of the nanoparticles. Electron dispersive spectroscopy (EDS) indicates that Zn and O are also present, but we cannot determine whether these are incorporated into the carbon matrix or exist as a separate, amorphous ZnO phase.

Comparing the e-beam behavior of IRMOF-1 with the other two zinc-containing MOFs demonstrates the crucial role of the metal coordination sphere in determining whether or not nanoparticles form, showing that nanoparticle growth conditions can be tuned using different linkers. In contrast to IRMOF-1, no ZnO is observed when MOF-508 is exposed to the 200 kV electron beam for any length of time. However, using the higher current densities available in the 400 kV electron beam, ZnO nanoparticles can be formed. The energy of the electrons in both TEM e-beams will initially ionize the materials along the electron track, after which the local excitation decays through various thermal and non-thermal routes to the ground state. The behaviors of the two MOFs indicate that the MOF-508 structure is more stable with respect to this excitation than IRMOF-1. In both MOFs Zn(II) is coordinated to four oxygen ions. The coordination geometry in IRMOF-1 (tetrahedral) is similar to the wurtzite ZnO structure. In MOF-508, the Zn(II) has a square-pyramidal paddlewheel configuration and is also coordinated to nitrogen

from the bipyridine linker. We therefore speculate that the greater stability of MOF-508 results from a combination of the additional energy required to rearrange the coordination sphere to create ZnO and improved radical stability as a result of the polycyclic bipy linker.



It is conceivable that nanoparticles of other zinc-containing **Figure 4.** TEM images and measured and simulated diffraction patterns of In nanoparticles. a) Larger nanoparticles, up to 100 nm in diameter, of In (dark contrast spots) form in the 400 kV electron beam. b) HRTEM image of polycrystalline/amorphous In nanoparticle. c) HRTEM image of a crystalline nanoparticle. Inset shows an FFT of the nanoparticle. d) Intensity map of simulated and measured diffraction patterns (shown in supporting information).

compounds could also form; both zinc nitride (Zn_3N_2 ; cubic) and carbide (ZnC) are known. However, exposing the nitrogen-only coordination sphere of ZIF-8 to both the 200 kV and 400 kV e-beams produces no detectable nanoparticles. Although it is possible these compounds could form in an amorphous state that is difficult to detect, it is also plausible that the low reactivity of the imidazole linker and/or the instability of Zn_3N_2 (known to react violently with water) prevent formation of phases other than ZnO.

In addition to the coordination sphere, the oxidation potential of the MOF metal ions determines whether an oxide or a metal nanoparticle will form, as illustrated in MIL-68(In) and Cu(BTC). In these structures, the metal ions are surrounded by oxygen sufficient to create stoichiometric indium and copper oxides, but instead these materials decompose to form the corresponding metal nanoparticles upon e-beam exposure. Traces of indium oxide are detected in the exposed MIL-68(In), but no copper oxides are found in the exposed Cu(BTC). This behavior is straightforwardly explained by the oxidation potentials of the three metals. Zn has the highest oxidation potential and is also one of the highest of any transition metal (0.76 V vs. SHE). It is therefore not surprising that in the presence of oxygen the nanoparticles derived from this growth method are ZnO. On the other hand, Cu has a much lower oxidation potential (-0.34 V vs. SHE), favoring formation of Cu nanoparticles. The structure of Cu(BTC) may also be advantageous, since two Cu atoms exist in close proximity in the paddlewheel structure. Indium has an oxidation potential between Cu and Zn with an oxidation potential of 0.34 V vs. SHE. This evidently allows In_2O_3 to form in small quantities, but EDS indicates this exists only as a surface layer (Figure S5), in agreement with previous reports.^{22,23} These results

suggest that a relatively sharp boundary in oxidation potential separates formation of metallic and oxide nanoparticles.

Cu(BTC) is very unstable in the beam, decomposing after 1 s to 2 s, too short to obtain SAED patterns. Within 3 s to 5 s in the 200 kV e-beam, Cu nanoparticles form with an average size of 2.7 nm \pm 0.5 nm based on analysis of 100 particles (Figure S4). These are among the smallest Cu nanoparticles with the narrowest size distribution reported to date.²⁴ Exposure to the 400 kV electron beam facilitates formation of much larger nanoparticles. A TEM image following a 30 s exposure reveals particles as large as 60 nm in diameter.

MIL-68(In) is similar to Cu(BTC), breaking down very quickly and forming In nanoparticles within 3 s to 5 s when exposed to the 200 kV electron beam. These particles are extremely small and nearly monodisperse, having an average diameter of 1.2 nm \pm 0.3 nm, making them also among the smallest reported (Fig. 3).

When MIL-68(In) is exposed to the higher current density of the 400 kV beam, In nanoparticles with diameters as large as 100 nm form (Figure 4a). High resolution TEM indicates that amorphous (Figure 4b), polycrystalline, and single-crystal (Figure 4c) morphologies are formed, as well as mixtures of these. Amorphous particles such as the one in Fig. 4b also have an amorphous shell (indicated by spots and ring pattern in the fast Fourier transform), which could be either In, as previously reported,²⁵ or carbonaceous material. An unexpected finding is that these large In nanoparticles, which lack any obvious grain boundaries, are composed of both face-centered cubic (fcc) and body-centered tetragonal (bct) phases. It is known that the crystal structure of In nanoparticles depends on size. Nanoparticles < 10 nm in diameter have an fcc structure,^{22,25,26} which due to its higher symmetry is more stable at the nanoscale.²² Nanoparticles > 10 nm diameter have the *bulk* bct structure. Nanobeam diffraction (NBD) analysis of individual nanoparticles clearly indicates that both fcc and bct phases are present in these particles (Figure S6). The intensities of the diffraction spots in simulated and measured diffraction patterns (Figure S6) are compared in Figure 4d. Reflections for fcc and bct phases nearly overlap, but are distinguishable, along with some In_2O_3 . Unfortunately, NBD cannot reliably indicate the relative amounts of these phases, but the fact that the fct phase is detected at all indicates that these domains are not the result of a minor impurity. As such, to our knowledge these are the largest fcc-In nanoparticles reported. The fact that this crystal structure is normally found in nanoparticles at least 10 times smaller suggests that coalescence is sufficiently rapid under these conditions for metastable crystal phases to form (see supporting information for more details).

The e-beam induced breakdown of MOFs very likely proceeds by a mechanism similar to that in organic materials, which is attributed to bond scission by means of secondary electron generation.²⁷ Localized heating plays essentially no role, as the temperature increase predicted by the Bethe equation is less than 10 K.⁶ Electron ionization mass spectra of carboxylic acids, a linker in four of the five MOFs investigated here, show that decarboxylation and dehydroxylation are the first and most abundant fragmentation events.²⁸ Decarboxylation will free the metal center from the rigid framework, presumably releasing CO_2 and allowing metal-ion coalescence to occur. The aromatic ring component of the linker that remains is unlikely to further fragment, based on extensive literature showing that aromatic compounds are much more radiation resistant than aliphatic compounds.^{29,30} However, loss of the carboxyl groups will create aromatic radicals that can undergo polymerization and H_2 loss to

form the carbonaceous material that surrounds the nanoparticles, some of which appears to be graphitic.

We also expect that the ease of decarboxylation is correlated with the metal-linker bond strength and may influence the type of nanoparticle that forms. To determine the metal-ligand bond strengths of the various MOFs, we employed density functional theory (DFT) to estimate the homolytic bond dissociation energies in these MOFs. Specifically, we calculated the dissociation of a single linker within a MOF-like cluster (see supporting information) according to the reaction $(L)_n\text{-M-L} \rightarrow (L)_n\text{-M}\cdot + L\cdot$, where $(L)_n\text{-M-L}$ refers to the cluster, $(L)_n\text{-M}\cdot$ is the remaining MOF radical fragment, and $L\cdot$ is the neutral linker radical. The calculations indicate that among the zinc-containing MOFs, the Zn-O bond in IRMOF-1 is the strongest, while the Zn-N coordination bond in ZIF-8 is the weakest. The Cu-COO bond energy in the Cu(BTC) cluster is also weak relative to IRMOF-1, which is consistent with its rapid degradation to form Cu nanoparticles. The overall order of bond strength is ZIF-8 (2.3 eV) \approx Cu(BTC) (2.5 eV) \ll MOF-508 (4.5 eV) $<$ IRMOF-1 (5.4 eV) $<$ MIL-68(In) (6.0 eV). Although these values should not necessarily be taken at face value, the trend is not fully consistent with the observed rate and nanoparticle composition, suggesting that the geometry and composition of the coordination sphere are the key factors in determining particle composition and rate of formation. MIL-68(In) is the exception, having both a strong In-O bond and a rapid rate of e-beam breakdown. As a main-group element, we expect its oxides to be very stable, so its rapid decomposition in the electron beam to form metallic In nanoparticles may be the result of a unique combination of structural factors. Additional experiments will be needed to achieve a clear understanding of these effects.

In conclusion, our results demonstrate that metallic and semiconducting nanoparticles can be synthesized using electron-beam irradiation of MOFs, using a TEM to monitor nucleation and growth in real time and with sub-nm resolution. Their type and morphology are determined by the metal oxidation potential, coordination sphere, and e-beam current density and energy. Following MOF decomposition, the residual carbonaceous material provides a stabilizing matrix that prevents nanoparticle agglomeration and reoxidation of metallic nanoparticles. This method can be extended to MOFs with different linkers and metal centers, providing a versatile route to a variety of nanoparticle compositions, phases, and morphologies. Although the size of the exposed area in our proof-of-concept experiments was limited by the diameter of the TEM beam, high-resolution writing and broad-area exposure are possible using currently available instrumentation. When combined with the ability to infiltrate materials into the MOF pores prior to e-beam exposure, as we previously demonstrated with silver,^{5,6} the potential to fabricate metallic and semiconducting nanoparticle heterostructures using MOFs as scaffolds or templates can be envisioned.

Disclaimer The full description of the procedures used in this paper requires the identification of certain commercial products and their suppliers. The inclusion of such information should in no way be construed as indicating that such products or suppliers are endorsed by NIST or are recommended by NIST or that they are necessarily the best materials, instruments, software or suppliers for the purposes described.

Acknowledgment: The authors thank Dr. Joshua Sugar for his technical assistance with various aspects of this project. This work was supported by the Laboratory Directed Research and Development Program at Sandia National Laboratories. Sandia is a multiprogram

laboratory operated by Sandia Corporation, a Lockheed Martin Company, for the United States Department of Energy's National Nuclear Security Administration under Contract DE-AC04-94AL85000.

Supporting Information Available: Additional TEM images, diffraction analysis and Raman and PL spectra. This material is available free of charge via the Internet at <http://pubs.acs.org>.

References

- (1) Burda, C.; Chen, X. B.; Narayanan, R.; El-Sayed, M. A., *Chem. Rev.* **2005**, *105*, 1025.
- (2) Bronstein, L. M., *Colloid Chemistry* **1** **2003**, 226, 55.
- (3) Hermes, S.; Schroter, M. K.; Schmid, R.; Khodeir, L.; Muhler, M.; Tissler, A.; Fischer, R. W.; Fischer, R. A., *Angewandte Chemie-International Edition* **2005**, *44*, 6237.
- (4) Moon, H. R.; Kim, J. H.; Suh, M. P., *Angewandte Chemie-International Edition* **2005**, *44*, 1261.
- (5) Houk, R. J. T.; Jacobs, B. W.; El Gabaly, F.; Chang, N. N.; Talln, A. A.; Graham, D. D.; House, S. D.; Robertson, I. M.; Allendorf, M. D., *Nano Lett.* **2009**, *9*, 3413.
- (6) Jacobs, B. W.; Houk, R. J. T.; House, S. D.; Robertson, I. M.; Talin, A. A.; Allendorf, M. D., *in press Chem. Sci.* **2010**.
- (7) Akcoltekin, E.; Peters, T.; Meyer, R.; Duvenbeck, A.; Klusmann, M.; Monnet, I.; Lebius, H.; Schleberger, M., *Nat. Nanotechnol.* **2007**, *2*, 290-294.
- (8) Sepulveda-Guzman, S.; Elizondo-Villarreal, N.; Torres-Castro, D. F. A.; Gao, X.; Zhou, J. P.; Jose-Yacamán, M., *Nanotechnology* **2007**, *18* (33).
- (9) Tanaka, M.; Chu, F.; Shimojo, M.; Takeguchi, M.; Mitsuishi, K.; Furuya, K., *Applied Physics Letters* **2005**, *86* (18).
- (10) Wei, X.; Wang, M.-S.; Bando, Y.; Golberg, D., *J. Am. Chem. Soc.* **2010**, *132*, 13592-3.
- (11) Shekhah, O.; Wang, H.; Strunskus, T.; Cyganik, P.; Zacher, D.; Fischer, R.; Woll, C., *Langmuir* **2007**, *23*, 7440-7442.
- (12) Yaghi, O. M.; O'Keeffe, M.; Ockwig, N. W.; Chae, H. K.; Eddaoudi, M.; Kim, J., *Nature* **2003**, *423*, 705-714.
- (13) Chen, B. L.; Liang, C. D.; Yang, J.; Contreras, D. S.; Clancy, Y. L.; Lobkovsky, E. B.; Yaghi, O. M.; Dai, S., *Angewandte Chemie-International Edition* **2006**, *45*, 1390-1393.
- (14) Park, K. S.; Ni, Z.; Cote, A. P.; Choi, J. Y.; Huang, R. D.; Uribe-Romo, F. J.; Chae, H. K.; O'Keeffe, M.; Yaghi, O. M., *Proceedings of the National Academy of Sciences of the United States of America* **2006**, *103*, 10186-10191.
- (15) Volkringer, C.; Meddouri, M.; Loiseau, T.; Guillou, N.; Marrot, J.; Ferey, G.; Haouas, M.; Taulelle, F.; Audebrand, N.; Latroche, M., *Inorganic Chemistry* **2008**, *47*, 11892-11901.
- (16) Chui, S. S. Y.; Lo, S. M. F.; Charmant, J. P. H.; Orpen, A. G.; Williams, I. D., *Science* **1999**, *283*, 1148-1150.
- (17) ESTAR database "Stopping powers and ranges for electrons," <http://physics.nist.gov/PhysRefData/Star/Text/method.html> National Institute of Standards and Technology web site, accessed Nov. 15, 2010.
- (18) Lee, J. J.; Bang, J.; Yang, H., *Journal of Physics D-Applied Physics* **2009**, *42* (2).
- (19) Vanheusden, K.; Warren, W. L.; Seager, C. H.; Tallant, D. R.; Voigt, J. A.; Gnade, B. E., *J. Appl. Phys.* **1996**, *79*, 7983-7990.
- (20) Huang, M. H.; Wu, Y. Y.; Feick, H.; Tran, N.; Weber, E.; Yang, P. D., *Adv. Mater.* **2001**, *13*, 113-116.
- (21) Jawhari, T.; Roid, A.; Casado, J., *Carbon* **1995**, *33* (11), 1561-1565.
- (22) Balamurugan, B.; Kruis, F. E.; Shivaprasad, S. M.; Dmitrieva, O.; Zahres, H., *Appl. Phys. Lett.* **2005**, *86* (8).
- (23) Zhao, Y.; Truhlar, D. G., *J. Chem. Phys.* **2006**, *125* (19).
- (24) Zhao, M. Q.; Sun, L.; Crooks, R. M., *J. Am. Chem. Soc.* **1998**, *120*, 4877-4878.
- (25) Oshima, Y.; Nangou, T.; Hirayama, H.; Takayanagi, K., *Surf. Sci.* **2001**, *476*, 107-114.
- (26) Yokozeki, A.; Stein, G. D., *J. Appl. Phys.* **1978**, *49*, 2224-2232.
- (27) Reimer, L., *Transmission Electron Microscopy: physics of image formation and microanalysis*. Springer: Berlin and New York, 1989.
- (28) Martinez, R. I., *Journal of Research of the National Institute of Standards and Technology* **1989**, *94* (5), 281-304.

Supporting Information

Electron Beam Synthesis of Metal and Semiconductor Nanoparticles Using MetalOrganic Frameworks as Ordered Precursors

Benjamin W. Jacobs, Ronald J.T. Houk, Bryan M. Wong, A. Alec Talin, Mark D. Allendorff

Methods

TEM: A JEOL 2010F field emission electron microscope operating at 200 kV was used for creating nanoparticles and materials characterization. It is equipped with an energy dispersive x-ray spectrometer (EDS, Oxford Inca X-Sight). The current density in this instrument was $10.3 \text{ A/m}^2 \pm 0.1 \text{ A/m}^2$, measured using a Faraday cup. Diffraction was done using nanobeam diffraction (NBD) or with selected area electron diffraction (SAED). A JEOL 4000EX with a LaB₆ source operating at 400 kV was used to study the effects of higher energy and beam current on the creation of nanoparticles. The current density could not be directly measured in this instrument. The phosphor viewing screen in the TEM can be used to measure the current density, and is displayed on the control panel of the instrument. The

JEOL 2010F beam current was directly measured using a Faraday cup and picoammeter. This current was compared to the phosphor view screen current density readout on the control panel. There exists a nearly linear relationship between the phosphor viewing screen readout and the actual measured beam current. This same ratio was used to estimate the beam current hitting the sample in the 4000EX, $\approx 730 \text{ A/m}^2$.

Sample preparation: For sample preparation, all MOFs were placed in ethanol and sonicated to create a dilute suspension. They were then deposited on copper TEM grids with a thin lacey carbon film support or on Si₃N₄ grids with a 50 nm thick window.

Raman Spectroscopy: Raman spectra were collected using a frequencydoubled Nd:YAG 532 nm laser with a $\approx 2 \text{ }\mu\text{m}$ diameter laser spot and an average power of $\approx 0.3 \text{ mW}$, and an Acton SpectraPro model 2750 0.75 m triple spectrometer.

Photoluminescence: Photoluminescence (PL) spectra were collected using a 325 nm wavelength He/Cd laser excitation source focused with a UV objective to a spot size of $\approx 5 \text{ }\mu\text{m}$ in diameter with average power of $\approx 1 \text{ mW}$ and an Ocean Optics USB-2000 spectrometer with $\approx 1 \text{ nm}$ spectral resolution.

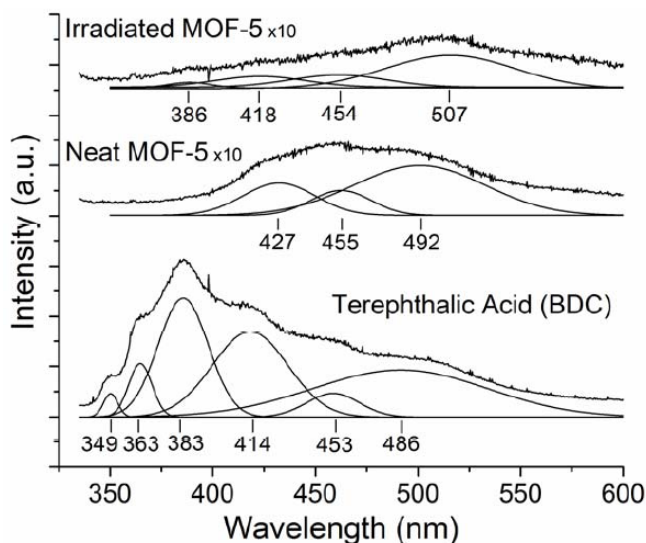


Figure S1. Photoluminescence spectra of BDC, neat MOF-5 and MOF-5 exposed to the electron beam.

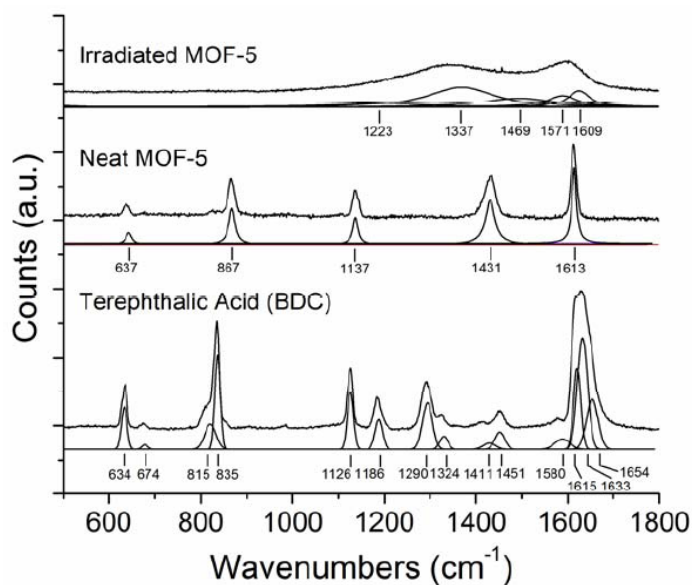


Figure S2. Micro Raman spectra of BDC, neat MOF-5 and MOF-5 exposed to the electron beam.

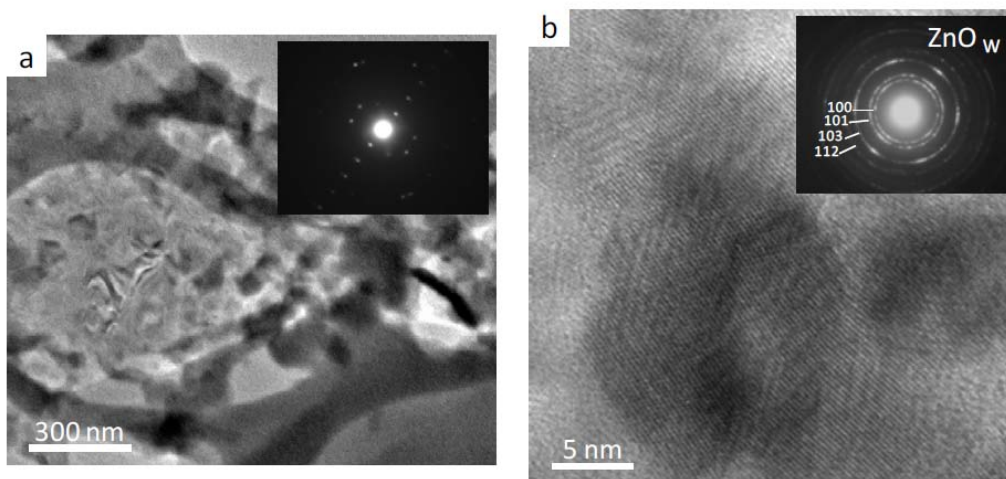


Figure S3. a) TEM image of MOF-508 after minimal exposure to the 200 kV electron beam. An SAED pattern, upper right inset, shows diffraction spots of the MOF, which corresponds to diffraction from the MOF crystal lattice and indicates the long range order of the framework. MOF-508 is somewhat more robust in the electron beam than MOF-5, the framework will hold up in the beam for tens of seconds while MOF-5 holds up for only a few seconds. b) A TEM image of MOF-508 after exposure to the 400 kV electron beam. The higher current density in this TEM allows for ZnO formation. The polycrystalline SAED pattern in the upper right inset was solved for the wurtzite crystal structure of ZnO.

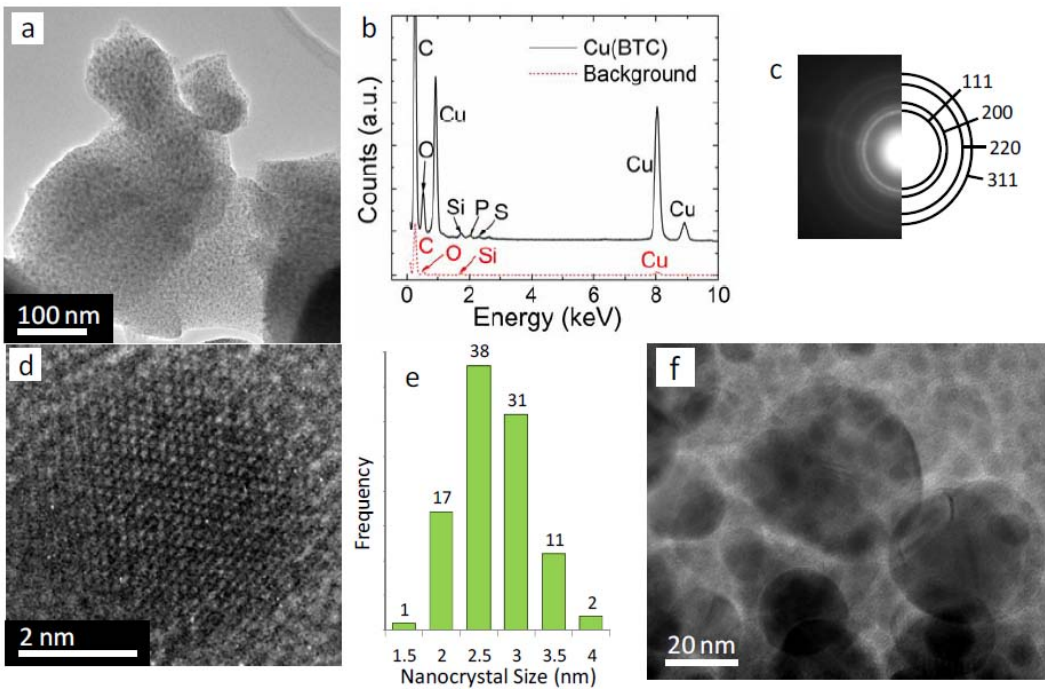


Figure S4. TEM images of Cu(BTC). a) Cu(BTC) after exposure to the 200 kV electron beam. The dark contrast spots correspond to Cu nanoparticles. b) Size distribution of the Cu nanoparticles. Their size was $2.7 \text{ nm} \pm 0.5 \text{ nm}$. c) An SAED pattern of the nanoparticles was solved for fcc Cu. d) High resolution TEM image showing a single crystal of Cu. e) EDS spectra of Cu(BTC) and the background. Si, P and S were contaminates from the TEM grid. A small portion of the Cu intensity is from the Cu TEM grid, but the majority comes from the Cu in the MOF.

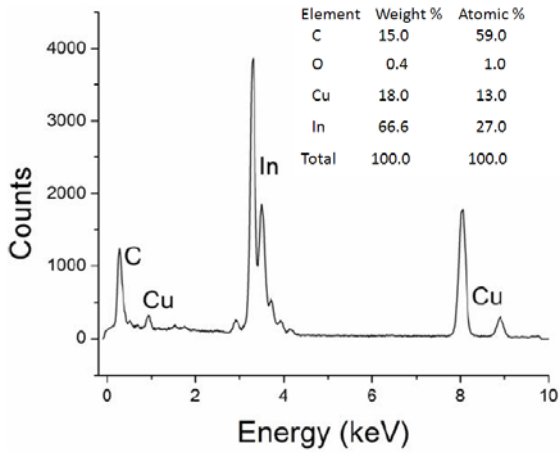


Figure S5. EDS spectrum of a single In nanoparticle. The inset shows the elemental composition of the nanoparticle. Oxygen is only a trace of the overall composition. Carbon is present due to the carbonaceous material in the MOF and the lacey carbon support film on the TEM grid. Copper is from the copper TEM grid. The uncertainty in the composition is $\pm 0.1 \%$ as determined using EDS standards.

fcc and A6 fct In nanoparticle formation

Since the formation of an apparently metastable In phase is unusual, we performed a more detailed structural analysis using nanobeam diffraction (NBD) analysis. NBD indicates that as many as three different phases can be present within the 100nm particles: two corresponding to metallic In and one to In_2O_3 . The metallic phases are body-centered tetragonal (bct) (equivalently described as A6 face-centered tetragonal) and fct ($a = 0.459 \text{ nm}$ and $c = 0.496 \text{ nm}$). The reported lattice parameter for the fcc phase vary from 0.471 nm to 0.5 nm .^{22, 24} In_2O_3 has a cubiotype lattice ($a = 1.011 \text{ nm}$). These structures are very similar and therefore difficult to distinguish, so we simulated the diffraction pattern in which all three crystal components are aligned along the $[011]$ zone axis (Figure S6), assuming an fcc lattice parameter of 0.5 nm . Diffraction spots of the three different crystals can be readily distinguished in the simulated pattern, even though they are in very close proximity. In the measured diffraction pattern, (Figure 4e), the spots corresponding to each crystal structure are best visualized using a one-dimensional intensity map (Figure 4f) obtained from data in the rectangular dotted areas of Figures 4d and 4e. Comparing the measured and simulated diffraction shows that the intensity and location of each spot in the simulated and real diffraction patterns are nearly identical. This suggests that there is a mixture of A6 fct and fcc In and fcc In_2O_3 in this nanoparticle. Some spots are smeared indicating polycrystalline components.

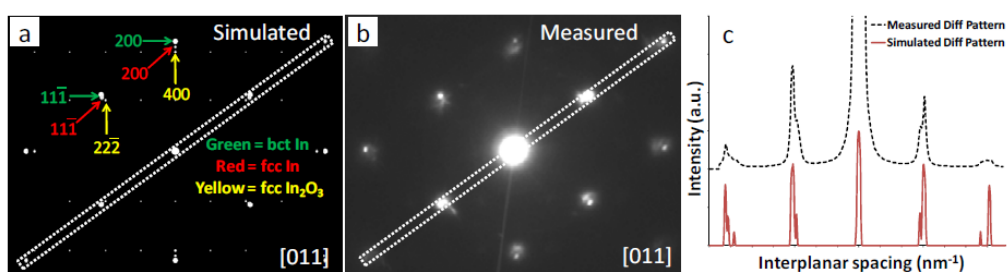


Figure S6. a) Simulated diffraction pattern of a crystal with all three bct and fcc In and fcc In_2O_3 crystal structures. b) Measured NBD diffraction pattern of an In nanoparticle. c) Intensity maps from the areas inside the dotted boxes in each diffraction pattern.

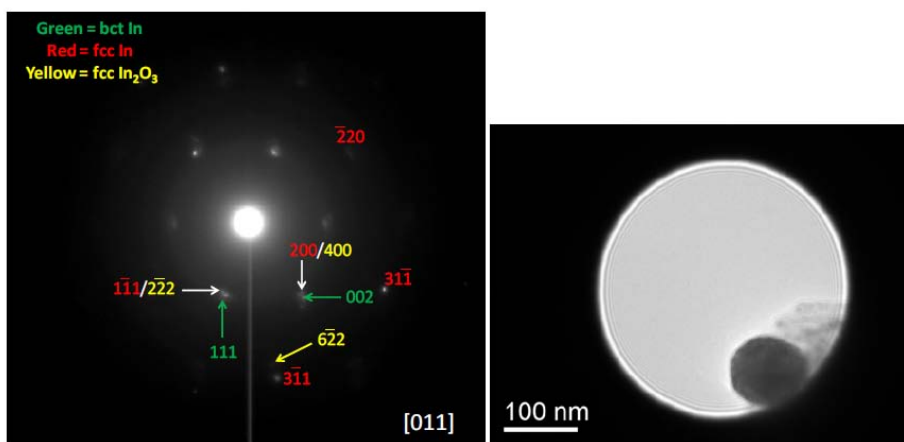
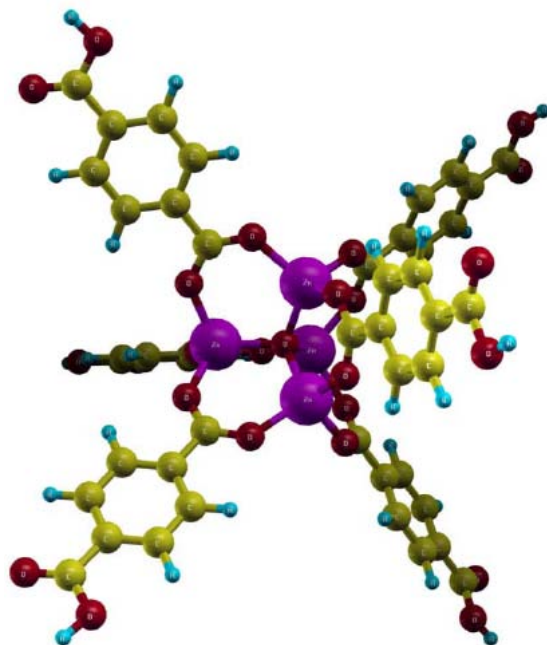
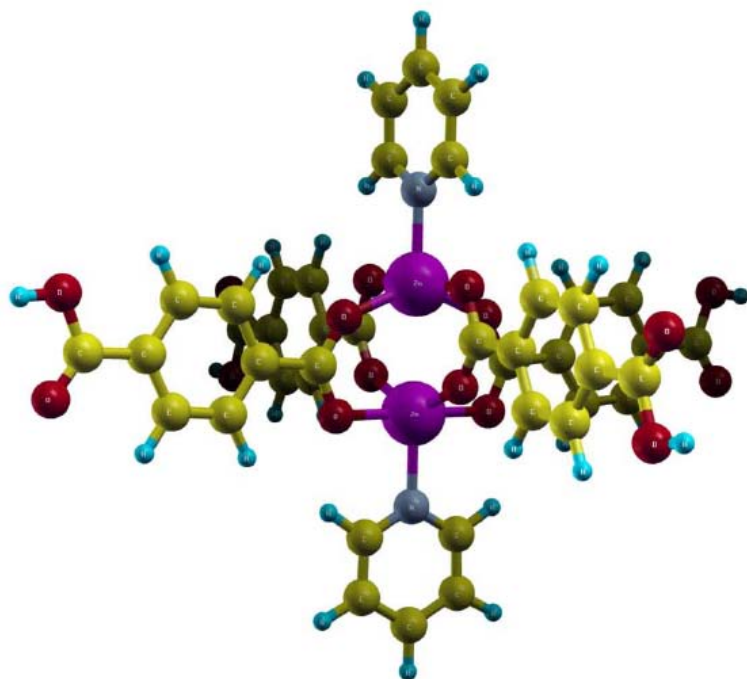


Figure S7. The left image shows a diffraction pattern of an individual In nanoparticle approximately 100 nm in size. All three components of fcc and bct In as well as In_2O_3 were observed. The In_2O_3 diffraction spots are weaker than the others indicating that there is less present in the nanoparticle.



MOF-5: $Zn_4O(C_8H_5O_4)_6$



MOF-508: $Zn_2(C_5H_5N)_2(C_8H_5O_4)_4$

ZIF-8: $\text{Zn}(\text{C}_4\text{H}_6\text{N}_2)_4^{2+}$

